Textural and mineral chemical evidence for the cumulate origin and evolution of high-titanium basalt fragment 71597

Patrick H. Donohue[1,*] and Clive R. Neal[1]

[1]Civil and Environmental Engineering and Earth Sciences, University of Notre Dame, Notre Dame, Indiana 46556, U.S.A.

Abstract

Basalt fragment 71597 is the sole high-titanium mare basalt showing evidence for olivine accumulation during formation. The petrogenesis of this unique sample was investigated using quantitative textural analysis and major- and trace-element mineral geochemistry. Crystal size distribution analysis identified two size populations of olivine, which we separate into cumulate and matrix olivine. The spatial distribution of olivine also supports clustering of olivine crystals, likely during accumulation. Observed mineral chemistry was consistent with an origin through olivine accumulation, although where this occurred cannot be discerned (e.g., in ponded melts at the base of or in the lunar crust, or within a thick high-Ti basalt flow). Attempts to place 71597 within a geochemical group were inconclusive both using subtraction of cumulate olivine from bulk composition, and by modal recombination of major phases. However, equilibrium liquid compositions of augite and plagioclase are determined to be consistent with an origin by fractionation from the Type B2 chemical suite of Apollo 17 high-Ti basalts. This method of classification has potential for placing other Type U ("Unclassified") basalts into chemical suites.

Keywords: Mare basalts, cumulates, crystal size distributions, LA-ICP-MS

Introduction

Olivine cumulates have been recovered from multiple lunar locales, although they form only a small part of the mare basalt sample collection. The majority of cumulates are low-titanium (TiO_2 < 6 wt%) composition comprising Apollo 12 ilmenite basalts 12005 and 12036 (Dungan and Brown 1977; Rhodes et al. 1977), several members of the Apollo 12 olivine basalt suite (Neal et al. 1994), Apollo 15 basalts 15385 and 15387 (Ryder 1985), Apollo 14 clast 14305,122 (Taylor et al. 1983), and six fragments in lunar meteorite NWA 773 (Jolliff et al. 2003). The only high-Ti cumulate is basalt 71597 (8.4 wt% TiO_2), a 12.35 g fragment collected with Apollo 17 mission rake samples (Murali et al. 1977; Warner et al. 1977). The composition and formation of this fragment relative to Apollo 17 high-Ti basalts provides information on an end-member of lunar volcanic textures.

Whole-rock analyses (major and trace element abundances) conducted by neutron activation techniques (Murali et al. 1977) and mineral compositions (major element) have been interpreted to indicate basalt 71597 experienced 24–27% olivine and possible minor ilmenite accumulation (Warner et al. 1977). The evidence for accumulation described by Warner et al. (1977) can be summarized in four main points:

- 71597 contains the highest whole-rock MgO content (15.8 wt%) and the highest modal olivine abundance (19.3%) of any high-Ti basalt.
- Whole-rock REE abundances are lower than, but sub-parallel to, typical Apollo 17 high-Ti basalts, indicating dilution by REE-poor olivine (± ilmenite).
- There is a bimodal distribution of olivine Fo-content between large, anhedral olivine cores and small "matrix" olivine grains (Fig. 1).
- It is unusual to find olivine crystals several millimeters in size in a coarse-grained matrix, as large olivine crystals within other Apollo 17 samples are typically found as phenocrysts in fine-grained basalts (e.g., 74275).

Warner et al. (1979) further suggested 71597 originated in a Type B flow (after Rhodes et al. 1976; separated into Types B1 and B2 by Neal et al. 1990). However, the small sample size of 71597 (12.35 g; Neal and Taylor 1993) and coarse grain size has precluded the determination of an incontrovertibly representative whole-rock analysis, which means that 71597 remains unclassified. Apollo 17 high-Ti basalts are classified into several groups (Types A, B1, B2, C, D, and U for "unclassified") on the basis of whole-rock geochemistry (Rhodes et al. 1976; Warner et al. 1979; Neal et al. 1990; Ryder 1990). Type A basalts contain 50–60% higher incompatible trace element abundances than the other groups (Rhodes et al. 1976). Types B1 and B2 basalts were split primarily on the basis of La/Sm ratios (Neal et al. 1990). Type C basalts contain high MgO and Cr_2O_3, and have less ilmenite on the liquidus at early stages of crystallization. The Type D group is defined by a single basalt fragment (,2144) from drive tube 79001, and has the highest MgO/TiO_2 ratio and lowest incompatible trace element abundance of any other classified Apollo 17 basalt (Ryder 1990). Classification schemes for Apollo 17 basalts are weighted toward incompatible elements, and are thus strongly affected by the amount of mesostasis and late-stage components sampled. This effect is more pronounced

* Present address: Hawai'i Institute of Geophysics and Planetology, University of Hawai'i at Manoa, 1680 East-West Road, POST 602, Honolulu, HI 96822 U.S.A. E-mail: phd2@alumni.nd.edu
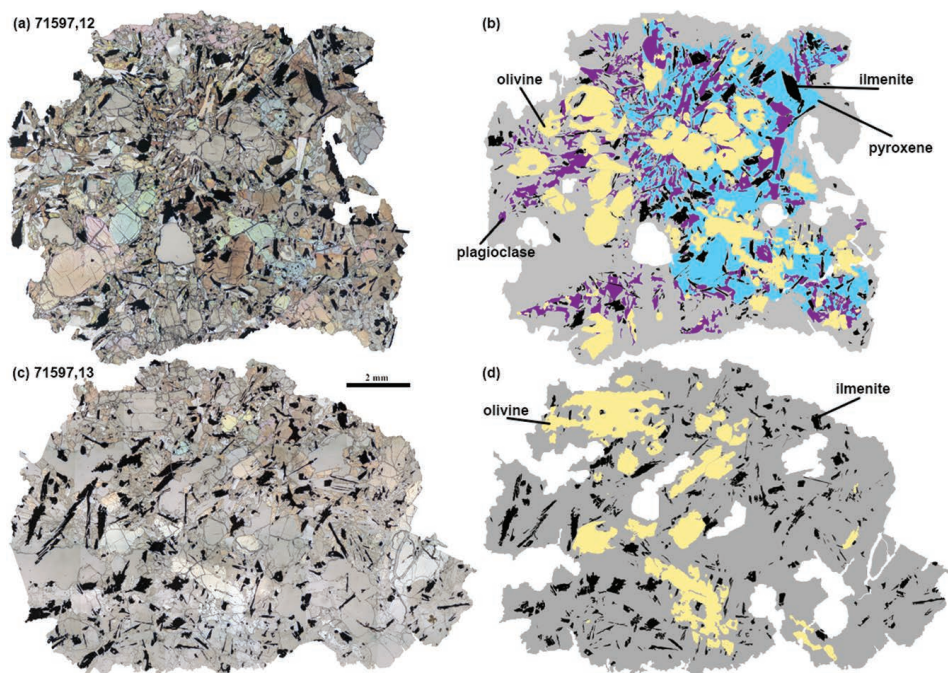
FIGURE 1. Plane-polarized light views and composites of traced phases of the two new thin sections of 71597. (**a**) 71597,12 and (**b**) composite of traced ilmenite (black), olivine (yellow), plagioclase (purple), and pyroxene (blue). Note pyroxene was only traced for half of the section. For (**c**) section 71597,13, only (**d**) ilmenite and olivine were traced. The more subdued color of olivine and pyroxene on the bottom half of 71597,13 is due to the lower thickness of the thin section. Crystals intersecting the edge of the sections were not traced. Gray areas in **b** and **d** represent the sample area. (Color online.)

in samples where <1 g material is used in bulk analyses (e.g., Haskin and Korotev 1977). Thus, the bulk composition of 71597 determined using a 0.61 g subsample (Murali et al. 1977) still may not be representative.

The explanation for the origin of 71597 given by Warner et al. (1977) favors the formation of large, skeletal olivine and ilmenite crystals toward the margins of a large flow that accumulate via gravitational settling toward the flow's interior. Other processes, such as mixing of magmas containing different crystal cargoes, have not been explored. Aspects of mare volcanic processes and the nature of olivine accumulation (e.g., gravitational settling during a single, large flow vs. magma mixing) can be addressed by mineral geochemistry and quantitative petrographic analysis. We present electron probe microanalysis and laser ablation inductively couple plasma mass spectrometry (LA-ICP-MS) analyses of mineral phases in two new thin sections of basalt 71597. Microscale details of basalt evolution are recorded in core-to-rim and inter-crystal compositional variations, and can best be constrained by in situ techniques. In addition, equilibrium liquid trace element compositions are used to constrain a petrogenetic model of magma evolution. We also undertake quantitative petrography on 71597 through Crystal Size Distribution (CSDs; Marsh 1988, 1998; Cashman and Marsh 1988; Higgins 2000, 2002, 2006; Higgins and Roberge 2003) and Spatial Distribution Patterns (SDPs; Jerram et al. 2003) analysis. Particularly relevant to this study is the work of Day and Taylor (2007) who demonstrated that a combined CSD-SDP approach could show not only variability in cooling rates, but also the importance of

clumping and formation of clustered crystal frameworks during the cooling of lunar lava flows. Additional studies have demonstrated the practicality of using the CSD technique to differentiate endogenous mare basalts from impact melts (Cushing et al. 1999; Neal et al. 2015), and the CSD-SDP methods to equate Apollo 17 samples with experimentally determined cooling rates (Donohue and Neal 2015).

SAMPLES AND METHODOLOGY

As noted above, the coarse grain size and small mass of 71597 has precluded an unambiguously representative whole-rock analysis. This represents an issue of obtaining representative CSD-SDP analyses of the sample due to its coarse grain size. To alleviate the effect of non-representivity when undertaking a textural analysis of 71597, two thin sections were requisitioned from sub-sample 71597,0 (designated 71597,12 and 71597,13) (Fig. 1). The data obtained from each thin section were combined where possible, allowing for a more robust statistical analysis.

Crystal Size Distribution (CSD) and Spatial Distribution Profile (SDP) methods

The application of CSD and SDP methods to lunar basalts has been discussed in detail in Day and Taylor (2007) and Donohue and Neal (2015). We present a brief summary here. Quantitative textural analyses were conducted on digital photomicrograph mosaics (Fig. 1). Crystal outlines were manually traced in the Adobe Photoshop program using reflected light photomosaics for ilmenite, and plane polarized light photomosaics for olivine, pyroxene, and plagioclase. Crystals larger than ~0.03 mm could be traced at the image resolution; smaller crystals were not included in the analyses due to issues with resolution and intersection effects, where grains smaller than the thin section thickness are underrepresented. Monomineralic layers were processed in the image-processing program "ImageJ" (ver. 1.44m) (Schneider et al. 2012) to determine crystal center coordinates (X,Y), major and minor crystal axis lengths and areas. Best-fit 3D crystal dimensions were estimated from a database of major and minor axis lengths, "CSDSlice" (Morgan

and Jerram 2006). Stereological corrections were made using the "CSDCorrections" (ver. 1.3.9) program (Higgins 2000) to calculate a semi-logarithmic CSD of population density vs. size. Crystal populations were split into size bins with five bins per decade (each size bin contains a range of crystal lengths 0.2 times larger than the previous). Using more than five bins per decade introduces errors because there are fewer crystals in each bin, and because more cycles of correction are needed during stereological conversion (Higgins 2000).

A reliable estimate of 3D crystal shape requires at least 75 total crystals (for tabular morphologies); a minimum of 250 crystals is recommended for more acicular shapes (Morgan and Jerram 2006). A size bin must contain three or more crystals to calculate upper and lower uncertainties on the population density. The "CSDCorrections" program calculates a goodness of fit (Q) of the data to a straight line, which allows for quantitative distinction between linear ($Q > 0.1$), sub-linear (Q between 0.001 and 0.1) and non-linear ($Q < 0.001$) CSDs (Higgins 2006). Sub-populations can also be isolated if a CSD appears kinked rather than curved. A CSD is considered kinked if the profile can be divided into two (or more) linear segments with unique slopes.

The CSD profile slope is a function of crystallization and is the inverse reciprocal of a characteristic crystal length (C_L) for a given population (Marsh 1988). The C_L is the product of growth rate (G) multiplied by residence time (τ). Growth rate is typically approximated based on experimental work and for a given phase may vary by several orders of magnitude between and even within specific studies (e.g., Burkhard 2005; Cabane et al. 2005; Vinet and Higgins 2010). For example, it us evident that temperature plays a critical role in growth rate (e.g., Burkhard 2005), which changes throughout crystallization. Thus, without additional knowledge of the system from which a phase crystallized, there are significant assumptions associated with residence time calculations and, therefore, potentially significant errors are introduced. Therefore, we do not use calculated absolute residence times as part of this study.

The mineral SDPs can be used to investigate the relative ordering and frameworks of mineral phases. Relative ordering is quantified by "R" values, where R is determined by comparing observed phase distributions to a similarly sized population of randomly packed spheres (Jerram et al. 1996, 2003). R can be compared to the percentage matrix (porosity) to distinguish touching from non-touching frameworks, as well as the relative ordering or clustering of phases. The SDP is a function of spatial relationships, and because we do not know exactly the separation of the two thin sections, the SDP is calculated for individual thin sections. Combining CSD and SDP analyses allows the effects of crystal nucleation and growth, magma mixing (Martin et al. 2006), and the relative position of a given sample in lava flows and intrusions (Jerram et al. 2003, 2010; Day and Taylor 2007; Donohue and Neal 2015).

Major and trace element analysis

Major element compositions of select ilmenite, pyroxene, plagioclase, and olivine crystals were obtained using a JEOL JXA-8200 electron microprobe at the Earth and Planetary Sciences Microanalysis Facility, Washington University in St. Louis (Missouri). The microprobe was equipped with five wavelength-dispersive spectrometers and a JEOL (e2v/Gresham) silicon-drift energy-dispersive spectro meter. Beam operating conditions were 15 kV accelerating potential, 25 nA probe current, and a 5 μm spot size. A defocused beam (~10 μm diameter) was used to avoid loss of volatiles (e.g., Na, K) during plagioclase analyses.

Compositional analyses of several large (>10 μm) melt inclusions in olivine and ilmenite crystals, as well as additional olivine (spot and line raster), armalcolite, and mesostasis analyses were obtained using a Cameca SX50 electron microprobe at the University of Chicago (Illinois; see Supplementary[1] Table S1). Line raster analyses were obtained across two large, partially resorbed olivines in 71597,12. Typical operating conditions were 15 kV accelerating potential and a 30 nA probe current and a 1 or 5 μm spot size (for oxides and silicates, respectively).

Trace element abundances of crystals were obtained using an Element2 inductively coupled plasma mass spectrometer (ICP-MS) coupled to a UP213 Nd:YAG laser ablation system at the Notre Dame Midwest Isotope and Trace Element Research Analytical Center (MITERAC, Notre Dame, Indiana). Laser operating conditions were 5 Hz repetition rate and 5 ns pulse duration to achieve <15 J/cm² fluence for 15–80 μm beam sizes. An optimum carrier gas (He) flow rate of 0.6 L/min was used to move ablated particles downstream to a "Y"-connection where it was mixed with Ar-gas and introduced to the mass spectrometer. The NIST SRM 610 (for olivine, ilmenite, and armalcolite) and NIST SRM 612 (for plagioclase and pyroxene) glasses (Pearce et al. 1997) were used for external calibration purposes. Detection limits (3σ) for pyroxene calculated in GLITTER (van Achterbergh et al. 2001) were 0.001–0.03 ppm for Y, Nb, Cs, La, Ce, Pr, Nd, Sm,

Eu, Tb, Dy, Ho, Er, Tm, Lu, Hf, Ta, Th, U; 0.03–1 ppm for Sc, Mn, Co, Ga, Rb, Zr, Ba, Gd, Yb, Pb; 1–5 ppm for Cr, Ni, Sr; 5–10 ppm for Ti; and >200 ppm for Ca. Detection limits for plagioclase were 0.03–1 ppm for Y, Sm, Eu, Dy, and Er, and similar to that for pyroxene for other elements. Analyses of ilmenite and olivine were performed in medium resolution (resolution = mass/peak width of ~4000) to reduce spectral interferences, but at the cost of reduced sensitivity. Thus, detection limits for elements in olivine and Fe-Ti oxides were 0.08–5 ppm for Sc, V, Co, Y, Zr, Sr, Hf, Ta; 5–20 ppm for Cr and Mn; 20–100 ppm for Ti and Ni in olivine; and 100–200 ppm for Ti in Fe-Ti oxides. The Ti-content obtained by microprobe was utilized as the internal standard for ilmenite and armalcolite; similarly, MnO was the internal standard for olivine, and CaO for plagioclase and pyroxene. Data were reduced using the GLITTER software, which allows for time-resolved background (~50 s) and signal (~60 s) selection. Cracks, inclusions, and adjacent phases were avoided using a combination of transmitted and reflected light prior to ablation and confirmed by time-resolved signal review.

RESULTS

Textural analysis

In general, the two new thin sections are petrographically similar to the detailed description given by Warner et al. (1977), although absolute mineral abundances differ. Manual point-counting of 71597,12 (3454 points over an area 67 mm²) shows the sample contains 37% pyroxene, 33% olivine, 15% plagioclase, and 15% opaques (ilmenite and trace armalcolite, spinel, and troilite). Warner et al. (1977) conducted point-counting over a larger area (~240 mm²), and report less olivine (19.3%), more plagioclase (28.3%), and other minor differences compared point-counting results for 71597,12. Visual estimates of bulk fragments 71597,0 and 71597,5 range from 19–30% olivine (Warner et al. 1977; Neal and Taylor 1993).

Olivine CSD profiles for 71597,12 and ,13 were previously presented in Neal et al. (2015). They are nearly identical and are multiply kinked, but the two largest size bins of the 71597,12 olivine CSD do not contain statistically significant numbers of crystals (n = 2 each) (Table 1; Fig. 2a). In addition, only 43 olivine crystals could be reliably traced in 71597,13, almost half the recommended minimum for CSD calculations (Morgan and Jerram 2006). A more robust CSD was created by combining the olivine populations (n = 161) of 71597,12 and ,13. The resulting CSD (Fig. 2a) is consistent with the individual sample CSDs with kinks at crystal lengths of ~0.4 and ~2.2 mm. However, the two largest size bins have the largest error and do not represent a statistically unique population, especially given the low number of crystals (n = 4) so we do not interpret this portion of the CSD as being a third distinct population of olivine crystals. Consideration of all crystals >0.4 mm in length yields a sub-linear CSD profile ($Q = 0.013$) with a C_L of 0.57 mm. To avoid over-interpretation of the CSD data, we only consider the olivine CSD as representing two populations (C_L of 0.07 mm and 0.57 mm) in further calculations.

Ilmenite CSD profiles of both thin sections are indistinguishable, and strongly concave upward ($Q << 0.001$) (Table 1, Fig. 2b). Linear regression through the steep and shallow segments of the ilmenite CSD profile yields slopes corresponding to characteristic lengths of 0.4 and 0.8 mm, respectively. The largest ilmenites (up to 1.1 mm as measured in thin section) are similar in habit to but not as large as the elongate skeletal ilmenite (up to 5 mm) reported by Warner et al. (1977). The CSD reconstructs 3D morphologies from 2D cross sections. So, given the X:Y:Z shape ratios calculated for ilmenite, the "true" length

of a randomly oriented prismatic grain would likely be larger than the observed length. In addition, the CSD breaks population density (number of crystals for the measured area) into a range of sizes. The points represent the largest size of crystals in each bin, such that the 6.4 mm bin represents the population of crystals of sizes ranging from ~4 to 6.4 mm. Therefore, the large crystal sizes observed by Warner et al. (1977) are represented in the analysis here.

Pyroxene and plagioclase CSDs for 71597,12 are sub-linear with Q of 0.001 and 0.01, respectively (Table 1, Figs. 2c–2d). The characteristic lengths range from 0.3–0.4 mm. There is also a downturn of the CSD profile at the smallest crystal sizes for pyroxene and plagioclase, a feature not observed in ilmenite or olivine CSDs. Pyroxene and plagioclase crystals extend to size bins below the estimated limit of resolution of the CSD technique, and so this downturn likely is due to an under-representation of these smaller crystal sizes.

Spatial distribution profiles were determined for pyroxene (porosity, $P = 64\%$, $R = 1.03$), plagioclase ($P = 89\%$, $R = 0.91$), ilmenite ($P = 94\%$, $R = 0.76$), and olivine ($P = 90\%$, $R = 0.59$) in thin section 71597,12 (Table 1). Multiple thin sections cannot be combined for SDPs, as can be done for CSDs, because the SDP calculation is based on nearest neighbor distances. These SDP results are presented in Figure 3 along with SDP results of several Apollo 17 high-Ti basalts (Donohue and Neal 2015). Olivine and pyroxene form a touching crystal framework in 71597 (Fig. 3). The higher abundance of olivine appears to have offset the ilmenite and plagioclase populations to higher densities compared to other high-Ti basalts. A similar relationship was observed in low-Ti basalts (Day and Taylor 2007).

Petrography and mineral chemistry

Representative analyses of silicate, Fe-Ti oxide, and melt inclusion compositions are presented in Tables 2 and 3 (all analyses

TABLE 1. Crystal size distribution data for major phases

Phase split(s)	Area (mm²)	Crystals	vol%	Slope1		y-int1		Slope2		y-int2		Shape parameters	R²	NND *average*	SDP *R* value
							Olivine								
,12	102.2	118	16.4%	−9.04	± 1.70	4.55	± 0.49	−2.48	± 0.10	1.27	± 0.12	1:1.4:2	0.80	0.345	0.59
,13	61.7	43	19.2%	−8.47	± 1.15	4.15	± 0.35	−2.07	± 0.13	0.81	± 0.25	1:1.5:2.3	0.81	n.a.	n.a.
,12 + ,13	163.9	161	17.5%	−13.41	± 0.45	5.12	± 0.12	−1.76	± 0.39	0.09	± 0.79	1:1.4:1.9	0.84	n.a.	n.a.
							Ilmenite								
,12	102.2	482	5.7%	−2.60	± 0.58	3.86	± 0.30	−1.53	± 0.17	2.29	± 0.49	1:1.25:7	0.78	0.116	0.76
,13	95.7	393	6.9%	−3.06	± 0.10	4.08	± 0.04	−1.63	± 0.21	1.73	± 0.59	1:1.7:6	0.73	0.113	0.65
,12 + ,13	197.9	875	6.3%	−2.28	± 0.30	3.57	± 0.15	−1.22	± 0.13	1.67	± 0.53	1:1.25:7	0.77	n.a.	n.a.
							Plagioclase								
,12	102.2	286	10.9%	−2.25	± 0.13	2.93	± 0.20	–		–		1:1.7:4.5	0.79	0.260	0.91
							Pyroxene								
,12	102.2	362	35.5%	−3.51	± 0.29	4.77	± 0.35	–		–		1:1.6:2.9	0.81	0.181	1.03

Notes: n.a. = not applicable; vol% = volume percent. Slope# and y-int# = slope and intercept of portions of CSD profiles representing different size populations. NND is nearest neighbor distance (mm) to crystal of same phase.
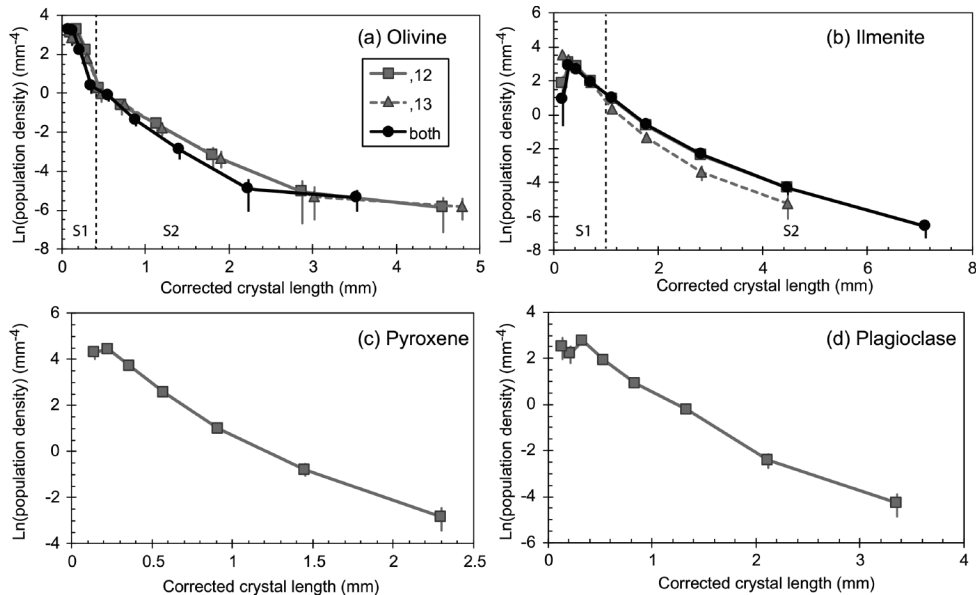

FIGURE 2. Crystal size distribution profiles for 71597,12 and ,13. (**a**) Olivine CSD profiles appear to be multiply kinked, and (**b**) ilmenite CSDs are concave upward. The CSD profiles are sub-linear for (**c**) pyroxene and (**d**) plagioclase. Error bars are 2σ based on counting statistics and may be smaller than the symbol size.
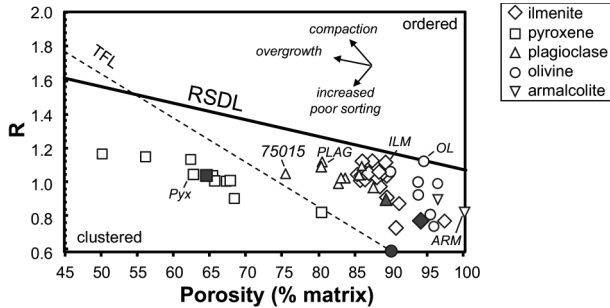
FIGURE 3. R-value (relative ordering) vs. Porosity (% matrix) for phases in Apollo 17 high-Ti basalts (open symbols; Donohue and Neal 2015) and basalt 71597,12 (filled symbols). RSDL = Random Sphere Distribution Line for modeled population of uniform spheres; points to the left of the Touching Framework line (TF) form a touching framework of crystals. Besides olivine in 71597, plagioclase in coarse-grained Type A basalt 75015 is the only other non-pyroxene phase to approach a clustered crystal distribution. The processes resulting in trends for related samples are included schematically. Figure after Jerram et al. (2003).

are available in Supplementary[1] Table S1). Large olivine crystals (Fo_{72-75}) typically exhibit normal zonation to higher-Fe margins (Fo_{66-72}) (Fig. 4). However, this zonation is less gradual at sharp olivine-olivine contacts or where mantled by titanaugite. Mantled olivines have a thin (<0.05 mm) reaction rim. The cores of large olivine crystals are compositionally distinct from cores of small olivine crystals (Fo_{62-68}). The data follow a crystal fractionation trend, wherein there is a corresponding decrease in Fo-content with decreasing Cr (698–1880 ppm) and V (17–55 ppm), and increasing Y (1.5–7.1 ppm) (Fig. 5). Compared to olivine from other mare basalt suites as well as olivine vitrophyres, 71597 olivines have unique compositions in terms of Ti/V and Cr/Y ratios on plots of Ti/V and Cr/V against Fo contents (Fig. 6).

Individual ilmenite compositions (n = 15) are homogeneous in regards to major element abundance, with the range in Mg# (12–19) representing inter-crystal variation (Fig. 7). Warner et al. (1977) noted a broader range in ilmenite Mg# of 4–29 (MgO = 1–8 wt%) from an unreported number of crystals. Paired core

and rim trace element analyses are also similar, with the exception of Co in one crystal in 71597,12 and Cr and Co in one crystal of 71597,13. In both cases, ilmenite rims show elevated Co abundance. There is inter-crystal variation, with a positive correlation between Zr (~110 to 750 ppm) and Hf (~5 to 20 ppm) (Fig. 7). Ilmenite typically contains blebs and lamellae of rutile and Al-rich chromite (too small for analysis by LA-ICP-MS), with inclusions of silicate melt, troilite, and/or Fe-metal.

The sole armalcolite crystal observed is partially rimmed by an ilmenite grain of average composition. The armalcolite crystal itself is at the low MgO (5.6 wt%) and high Al_2O_3 (2.0 wt%) range of armalcolite compositions in Apollo 17 mare basalts (Dymek et al. 1975; Papike et al. 1974; Warner et al. 1975; Warner et al. 1976a). Stanin and Taylor (1980) experimentally constrained the relationship between the Fe/Ti^{3+} component and oxygen fugacity in armalcolite. Our calculation of the Ti^{3+} component yielded an average oxygen fugacity, relative to the iron-wüstite (IW) buffer, of IW-0.66 ± 0.2. This is within the range determined for high-Ti basalts collected during the Apollo 17 mission, where armalcolite f_{O_2} was found to range from IW-0.4 to IW-0.8 (Stanin and Taylor 1980).

Pyroxene compositional variability is similar to that observed in Apollo 17 plagioclase-poikilitic mare basalts (Fig. 8, Table 3). Titanaugite is present as discrete crystals and as mantles (up to 0.3 mm) on olivine. Pigeonite is limited to extreme margins of augite and small crystals near the margins of partially resorbed olivine. There is only minor Fe-enrichment (up to Fs_{35}) in the crystals investigated here, although Warner et al. (1977) found ~5 pyroxenes with up to Fs_{50}. The Al/Ti ratio decreases from 2.4:1 in augite to ~2:1 in augite rims and pigeonite crystals, and the absolute abundance of Al_2O_3 and TiO_2 also decreases from core to rim in individual crystals. Augite REE profiles are subparallel and convex upward with strong negative Eu anomalies (Eu/Eu*, where Eu* = $\sqrt{[Sm_{CN} \cdot Gd_{CN}]}$, "CN" = CI Chondrite Normalized) (Fig. 8). Pigeonite and augite crystals are LREE depleted and have steep profiles from La-Sm, and relatively flat HREE profile. The La-Sm slope decreases with increasing total LREE abundance.

Plagioclase exhibits minor core-to-rim compositional zonation from An_{90} to An_{84} (Fig. 4). Poikilitic plagioclase grains
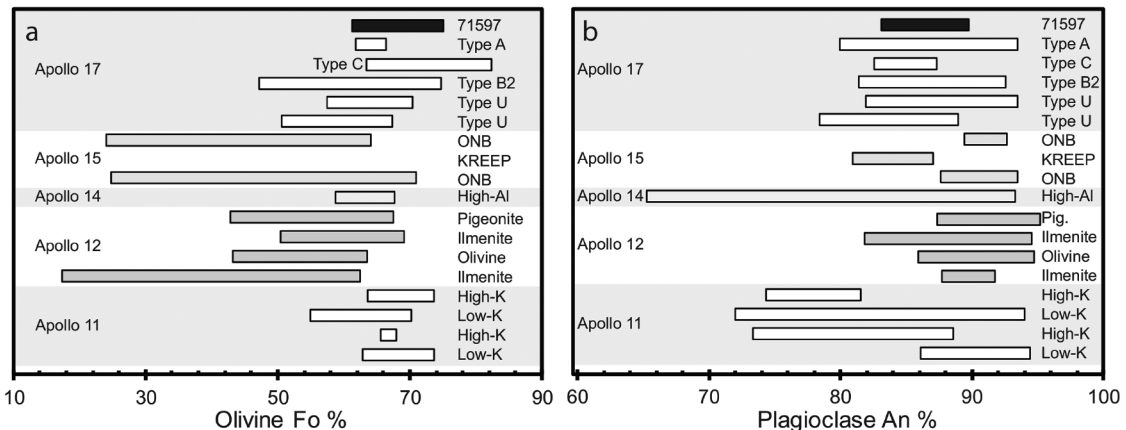

FIGURE 4. Ranges of (**a**) olivine Fo and (**b**) plagioclase An compositions observed in 71597 compared to literature values for individual samples of other lunar basalt types. Data from Fagan et al. (2013), Hallis et al. (2014), Schnare et al. (2008), and Neal and Taylor (1990).

TABLE 2. Average olivine and Fe-Ti oxide mineral chemistry for 71597 and for mare basalt groups

Phase	Large olivine core	2σ	Large olivine rim	2σ	Matrix olivine core	2σ	Ilmenite average	2σ	Armalcolite average	2σ	A17 Type A, B1, B2, C, U Olivine	A17 Ilmenite	A11 low-K, high-K Olivine	A11 Ilmenite	A12 Ilm, Ol, and Pigeonite suites Olivine	A12 Ilmenite	A14 high-Al and Ol. vitrophyre Olivine	A14 Ilmenite	A15 KREEP and Ol normative Olivine	A15 Ilmenite
n =	8		8		4		14		2											
wt%																				
SiO$_2$	37.7	(0.7)	37.3	(0.8)	36.9	(1.6)					24.7–41.0	0.01–0.38	29.2–38.6	0.12–0.23	33.4–39.9	0.03–8.90	35.7–42.3	0.16	27.2–48.2	b.d.–3.42
TiO$_2$							54.4	(2.0)	73.2	(1.4)	0.03–0.48	50.6–56.1		52.1–53.0	b.d.–0.20	43.7–54.3	0.01–0.15	53.24	0.01–1.03	39.7–52.9
Al$_2$O$_3$							0.04	(0.02)	2.03	(0.04)	b.d.–0.47	b.d.–0.62	b.d.–0.3	0.52–2.12	b.d.–0.74	b.d.–1.13	b.d.–0.21	0.09		0.03–1.28
Cr$_2$O$_3$	0.21	(0.06)	0.18	(0.08)	0.15	(0.02)	0.73	(0.26)	1.39	(0.15)	0.04–0.37	0.15–1.11	0.02–0.28		0.05–0.74	b.d.–0.75	b.d.–1.39	0.35	b.d.–0.51	b.d.–1.08
FeO	25.4	(2.9)	27.8	(2.6)	30.7	(2.4)	39.9	(2.5)	17.6	(1.1)	15.6–46	34.8–46.4	25.4–68.7	44.4–45.1	20.7–65.3	41.7–47.3	11.6–41.8	45.3	22.6–67.8	42.5–56.7
MnO	0.28	(0.05)	0.29	(0.05)	0.33	(0.12)	0.37	(0.07)	0.07	(0.04)	0.18–0.48	0.3–0.59	0.22–1.10	0.45	b.d.–0.52	0.27–0.43	0.10–0.42	0.47	0.26–0.75	0.19–0.39
MgO	36.1	(3.0)	34.1	(2.4)	31.9	(2.4)	4.5	(1.0)	5.54	(0.1)	19.5–44	0.1–8.7	0.5–36.5	0.75–1.35	3.54–40.1	b.d.–3.17	23.6–48.7	0.72	0.45–34.4	0.04–2.12
CaO	0.26	(0.02)	0.26	(0.03)	0.26	(0.03)					0.2–0.78	0.06–0.44	0.26–0.33	0.01–0.10	0–0.34	b.d.–2.51	0.03–0.85	0.05	0.24–11.7	0.004–0.36
Total	100.05	(0.73)	100.07	(0.94)	100.26	(1.14)	99.91	(0.96)	99.85	(2.22)										
Ol.Fo%	72	(4)	69	(3)	65	(3)					37–82		1–73.3		9–78		50–88		1.22–70.5	
Ilm Mg#							17	(3)	36	(2)		0.22–29		2.9–5.1		0–11.9		2.8		0.10–8.12
ppm																				
Sc	15	(8)	14	(9)	18	(7)	101	(20)	233	(24)	7.73–15.0	83–104		123	4.42–85.6		1.31–37.18		7.9–44.5	17.2–32.9
Ti	462	(142)	417	(112)	584	(357)	412	(254)			219–962				102–865		30.7–3028		122–2930	
V	43	(21)	33	(23)	24	(13)	3741	(2349)	1399	(118)	26.4–51.5			107	20.5–157		9.95–121		27.1–316	47.5–153
Cr	1299	(642)	1061	(514)	946	(489)	2391	(725)	7655	(1074)	991–1991	132–163			530–4840		140–3698		675–6047	532–1601
Mn	2129	(441)	2196	(436)	2581	(912)	8	(9)	753	(90)	1358–2202				1626–5208		589–3245		1970–4028	1841–3309
Co	65	(16)	63	(28)	71	(26)			20	(2)	39.5–56.8	20.9		24	80.6–238		14.7–85.6		86.2–148	22.7–29.2
Ni	35	(20)	23	(6)							21.7–68.8				6.55–500		4.17–362		38.8–203	4.4–6.3
Zn							3	(1)							1.58–6.94					
Y	3	(3)	4	(2)	5	(3)	426	(843)	233	(4)	0.18–2.14				0.14–3.66		0.03–72.1		0.2–4.7	1.7–8.2
Zr			2	(2)	2	(2)	51	(178)	32	(1)					b.d.–0.65				0.1–3.7	289–1127
Nb							19	(50)	12	(2)					b.d.–0.37				0–0.1	43.2–75.8
Hf							3	(7)	3	(4)		17.4		11	b.d.–0.02				0–0.2	6.9–18.1
Ta							2	(3)				4.9			b.d.				0	4.0–5.9
Sr									b.d.						b.d.–0.43				0–3.0	2.1–2.3

Notes: b.d. = below detection limit; 2σ = two standard deviation of average value listed. Literature data from Vobecký et al. (1971); Papike et al. (1974, 1976); Dymek et al. (1975); Warner et al. (1975, 1976a, 1976b, 1977); Walker et al. (1976); Haskin and Korotev (1977); McCallum and Charette (1978); Neal et al. (1990); Schnare et al. (2008); Fagan et al. (2013); Alexander et al. (2014); and Hallis et al. (2014).

contain 250–660 ppm Sr and 13–95 ppm Ba. One small grain (~0.2 mm; An$_{84}$) in a partially resorbed olivine grain contains 1100 ppm Sr and 250 ppm Ba. REE profiles are typical for lunar basalts, with large positive Eu-anomalies of 42 to 83. The LREE profiles are flat, and inter-crystal REE-abundance varies by an order of magnitude (Fig. 8).

Silicate melt inclusions are common in large, partially resorbed olivine crystals (>20 melt inclusions in some olivines) and are ubiquitous in ilmenite laths. These melt inclusions generally range in size from <0.01 to 0.05 mm. The majority of melt inclusions in olivine are microcrystalline intergrowths of pyroxene and plagioclase, with occasional anhedral troilite or ilmenite. Melt inclusions in ilmenite are generally glassy and occasionally contain troilite. Compositions were determined by microprobe only (Supplementary[1] Table S1) as the inclusion size precluded trace element determinations by LA-ICP-MS. There was some degree of host control on melt inclusion composition, where one melt inclusion in ilmenite contained lower TiO$_2$ compared to those in olivine and spinel, and one inclusion in spinel contained higher Cr$_2$O$_3$ than others. The largest melt inclusion (0.08 mm) was heterogeneous, with two separate analyses of 6.5 (center) and 4.5 (rim) wt% MgO. We did not have access to a heated stage to rehomogenize these inclusions but this remains as an avenue for future study.

DISCUSSION

Evidence of crystal accumulation

Using the methodology of Longhi et al. (1978) to calculate the equilibrium olivine composition for a given bulk composition, the Fe/Mg partition coefficient between melt and olivine was adjusted for TiO$_2$ content (Delano 1980). The equilibrium olivine composition calculated for 71597 using the bulk composition from Murali et al. (1977) is Fo$_{83}$, which is not observed in this sample (Warner et al. 1977; this work). This suggests the bulk composition is not representative of a liquid composition as the MgO abundance is inflated due to olivine accumulation.

Jerram et al. (2003) have used SDP textural analysis to define crystal frameworks that have high melt porosity and are loosely packed (produced from a mixed population of irregular-shaped clusters or clumps of crystals), and more tightly packed frameworks with lower melt porosity (produced from individual crystals). Figure 3 evaluates 71597 petrography in terms of R and porosity, comparing the mineral data to those from other Apollo 17 high-Ti basalts

TABLE 3. Average compositions of pyroxene and plagioclase compared to major mare basalt groups

Phase	Augite		Pigeonite		Plagioclase		A11 low-K and high-K		A12 Ilm, Ol, Plag basalts		A14 KREEP and high-Al		A15 KREEP and ONB		A17 Type A, B1, B2, C, U	
Analysis	average	2σ	average	2σ	average	2σ	Pyroxene	Plagioclase	Pyroxene	Plagioclase	Pyroxene	Feldspar	Pyroxene	Feldspar	Pyroxene	Feldspar
n =	13		5		19											
wt%																
SiO_2	48.7	(3.6)	51.6	(3.6)	47.3	(1.5)	44.1–52.5	45.7–53.3	45.0–53.5	44.3–48.2	45.3–51.3	42.8–49.5	41.2–54.0	43.1–48.5	38.1–78.5	45.5–52.4
TiO_2	3.52	(1.79)	1.33	(1.79)	0.13	(0.07)	0.72–3.74	0.5	0.35–2.64	0.03–0.16	0.84–1.62	0.02–0.11	0.19–3.99		0.26–14.1	0.03–0.32
Al_2O_3	4.78	(2.75)	1.67	(2.75)	32.7	(1.42)	0.57–5.25	17.2–34.5	0.66–7.90	30.9–35.7	1.20–3.01	31.3–36.0	0.26–11.9	30.1–34.6	0.42–23.4	0.11–34.5
Cr_2O_3	0.91	(0.40)	0.39	(0.40)	–		0–0.61	0.04	0–1.54		0–0.73		0–1.44		0.04–1.12	
FeO	9.4	(3.8)	18.9	(3.8)	0.45	(0.2)	9.6–45.8	0.30–2.8	12.9–46.5	0.49–1.85	15.4–34.7	0.07–0.99	12.9–45.9	0.37–1.06	2.31–48	0.28–32.9
MnO	0.22	(0.10)	0.36	(0.10)	–		0–0.67	0.05	0–0.56	<0.05	0–0.53		0.18–0.80		0–0.62	
MgO	14.4	(2.7)	18.8	(2.7)	0.30	(0.1)	1.40–22.0	0.07–2.5	0.29–24.3	0.01–0.51	0.57–21.2	0.03–0.38	0.15–26.3	0.15–1.16	0.27–24.4	0.01–0.31
CaO	17.8	(5.0)	6.61	(5.0)	17.2	(1.0)	3.52–18.8	11.7–18.6	2.61–16.9	16.3–19.2	4.37–18.2	15.6–19.4	2.02–18.2	16.3–19.0	0.75–20.7	0.11–17.4
Na_2O	0.07	(0.04)	0.02	(0.04)	1.35	(0.32)	0–0.12	0.55–2.70	0–0.05	0.40–1.72	0–0.09	0.41–2.21	0–0.12	0.70–1.67	0–0.55	0.78–2.45
Total	99.86	(1.17)	99.78	(1.17)	99.41	(1.17)										
Mg#	73	(4)	64	(4)	55	(13)	5–73	18–54	1–72	1–54			18–75			
En	44	(6)	55	(6)	–		0.6–63.4		0.41–67.0		5.8–63.7		1.9–80.1		0.9–67.1	
Fs	16	(6)	31	(6)	–				22.1–80.5						13.3–91.1	
Wo	40	(12)	14	(12)	–		0.55–43.5		6.55–42.2		7.5–33.7		2.6–36.2		5–49.3	
An	–		–		88	(3)		72.2–94.0		82.3–95.6		65.1–96.2		81.4–93.4		35.6–93.4
ppm																
Sc	196	(270)	220	(270)	b.d.	(270)	133	10.1	32–207	2.8–7.1			21.6–168	1.7–3.5	54–129	1
Ti	22566	(10445)	8432	(10445)	857	(290)			2840–16400	266–825			1409–12596	166–418		
Cr	4521	(1617)	1945	(1617)	6	(3)			132–22000	1.5–26.7			20.2–18636	2.4–13.9		
Mn	1437	(483)	591	(483)	57	(7)	22	8.5	760–8480	50.5–107			416–8191	42.7–83.2		
Co	10	(5)	12	(5)	0.4	(0.3)	22		10–159	b.d.–1.7			7.7–140	0.3–1.6	14–24	0.84
Ga	1.2	(0.4)	0.7	(0.4)	11	(26)						2.3–85	0.3–2.3	4.2–13.3		
Sr	9.7	(3.5)	4.0	(3.5)	381	(414)	400		0.32–24	221–629		23.5–420	0.2–21.9	136–503		
Y	32	(9)	24	(9)	0.5	(1)			3.3–153	0.23–2.13		0.14–17.7	1.6–373	0.1–0.4		
Zr	25	(14)	11	(14)	b.d.				1.2–158	b.d.–5.6			0.7–156	0.02–0.53		
Nb	0.09	(0.07)	0.07	(0.07)	0.02	(0.02)			0.4–3.5	b.d.–0.78			0–1.5	0.01–0.02		
Ba	0.05	(0.03)	0.06	(0.03)	38	(112)	230	210	0.6–40	13.4–103		4.47–464	0–57.1	9.4–56.9		
La	0.31	(0.16)	0.14	(0.16)	0.36	(0.93)	12.2	16.4	0.05–4.21	0.28–1.29		0.18–7.7	0–1.9	0.1–0.5		0.84
Ce	1.63	(0.53)	0.78	(0.53)	0.98	(2.64)	30	47	0.11–10.6	0.59–2.46		0.44–14.2	0–9.5	0.4–1.3		2.6
Pr	0.46	(0.12)	0.23	(0.12)	0.14	(0.37)			0.08–2.51	b.d.–0.36			0–2.6	0.04–0.15		
Nd	3.64	(0.90)	1.83	(0.90)	0.70	(1.64)		45	0.29–18.1	b.d.–1.43		0.22–18	0.1–22.2	0.2–0.7		
Sm	2.34	(0.63)	1.23	(0.63)	0.21	(0.54)	11.2	7.1	0.33–10.5	b.d.		0.04–5.8	0–15.4	0.1–0.2	0.99–5.1	0.59
Eu	0.21	(0.06)	0.08	(0.06)	3.09	(5.35)	1.2	1.8	0.09–0.56	1.29–4.52		0.40–3.3	0–1.0	0.8–3.4	0.10–0.45	5.34
Gd	4.38	(1.35)	2.78	(1.35)	0.19	(0.27)		1.4	0.42–18.1	b.d.		0.09–51	0.1–33.0	0.04–0.15		
Tb	0.81	(0.22)	0.51	(0.22)	0.04	(0.06)	3.3		0.10–3.69	b.d.			0–7.8	0.01–0.02		
Dy	6.17	(1.74)	4.24	(1.74)	0.13	(0.21)	20		0.64–27.2	b.d.		0.03–2.6	0.2–58.5	0.02–0.10	0.42–2.0	0.09
Ho	1.30	(0.34)	0.96	(0.34)	0.02	(0.04)	3.3		0.10–6.16	b.d.–0.08			0.1–14.2	0.01–0.02		
Er	3.65	(0.93)	2.96	(0.93)	0.06	(0.08)			0.30–17.8	b.d.–0.21		0.03–9.3	0.2–41.6	0.05		
Tm	0.53	(0.16)	0.46	(0.16)	0.02	(0.01)	4.6	1.3	0.08–2.83	b.d.						
Yb	3.55	(0.78)	3.27	(0.78)	0.08	(0.09)	11.2	5	0.44–21.2	b.d.–0.25		0.03–2.5	0.2–40.5	0.07	2.4–7.2	0.27
Lu	0.47	(0.14)	0.49	(0.14)	0.012	(0.00)	1.65	0.56	0.09–3.27	b.d.			0–5.8	0.011–0.012	0.37–0.92	0.034
Hf	1.75	(0.96)	0.79	(0.96)	b.d.		5.5	5	0.18–8.26	b.d.–0.21			0–6.4		0.58–1.2	0.15

Notes: Dashes indicate element not analyzed; b.d. = below detection limit. Literature data from Hodges and Kushiro (1974); Papike et al. (1974, 1976); Dymek et al. (1975); Warner et al. (1975, 1976a, 1977); Haskin and Korotev (1977); Neal et al. (1990); Schnare et al. (2008); Hui et al. (2011); Alexander et al. (2014); and Hallis et al. (2014).
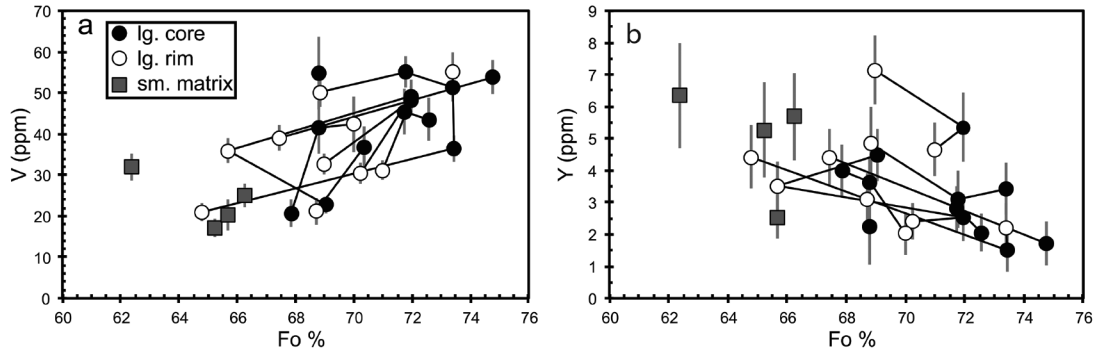
FIGURE 5. Element variation diagrams for large olivine interiors (filled) and rims (open symbols) as well as matrix olivine depicting (**a**) decreasing V (ppm) with melt evolution, and (**b**) corresponding increase in Y (ppm) abundance. Vertical lines indicate 1σ errors. Multiple analyses of individual crystals are connected with a gray line.
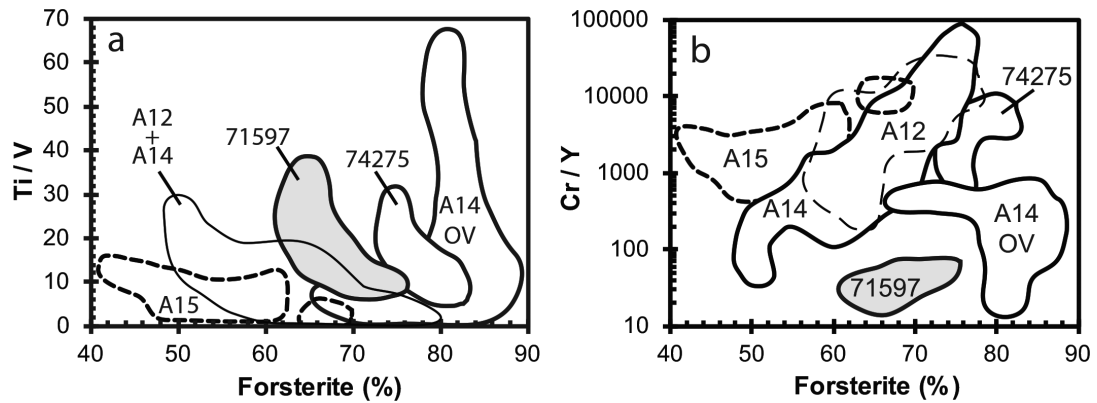

FIGURE 6. Olivine forsterite variability vs. (**a**) Ti/V and (**b**) Cr/Y vs. olivine forsterite contents. Fields drawn from literature: Apollo 12 (A12) ilmenite basalts, pigeonite basalts, olivine basalts, Apollo 14 (A14) Groups A, B, and C basalts, Apollo 14 olivine vitrophyres (OV), and Apollo 17 sample 74275 from Fagan et al. (2013); Apollo 15 (A15) olivine normative and quartz normative basalts from Schnare et al. (2008).
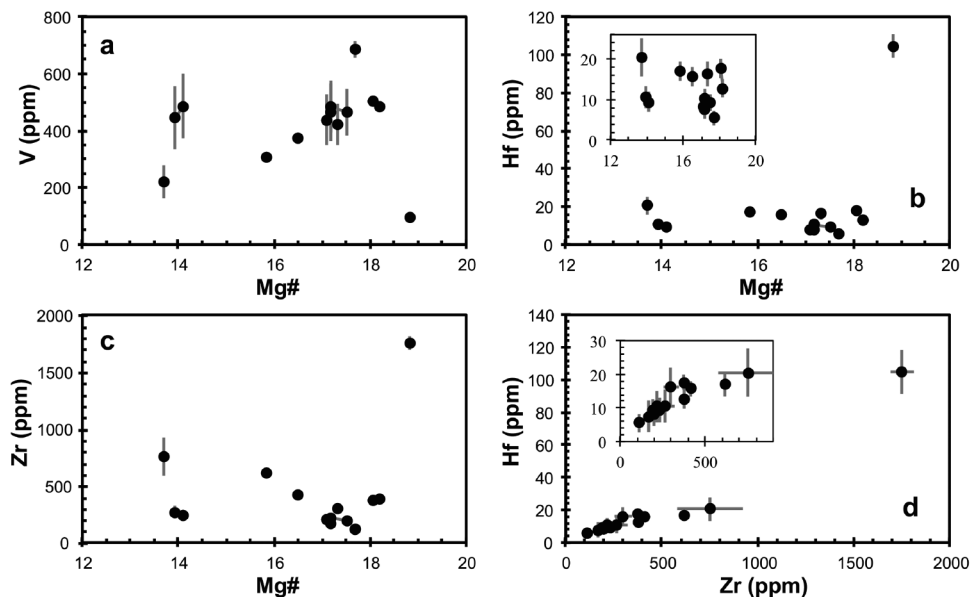
FIGURE 7. Ilmenite major and trace element variation diagrams. 1σ errors for trace elements indicated for each point where larger than the symbol.
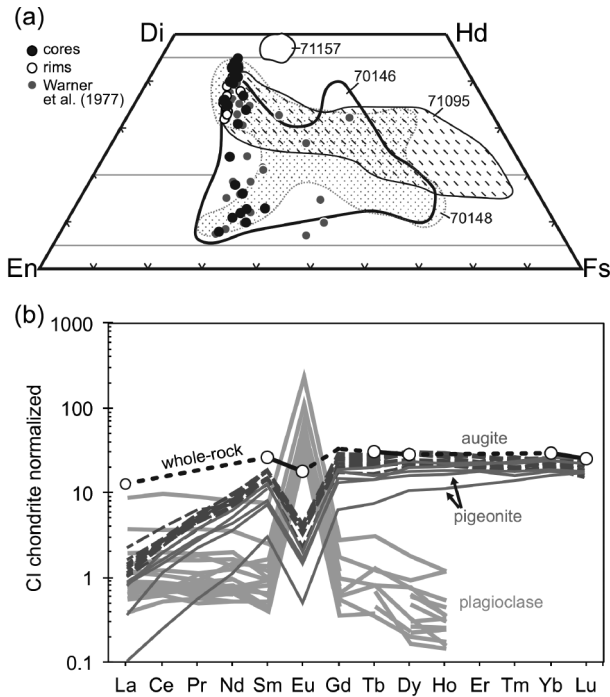
FIGURE 8. (**a**) Composition of pyroxene projected onto pyroxene quadrilateral with data from Warner et al. (1977) for comparison. (**b**) REE profiles of augite, pigeonite, and plagioclase of 71597 are typical of Apollo 17 basalts. Whole-rock values from 71597,1 (Murali et al. 1977). Values for CI chondrite from McDonough and Sun (1995).

(Donohue and Neal 2015). Pyroxene is the most abundant groundmass phase in the Apollo 17 high-Ti basalts (e.g., Dymek et al. 1975; Neal et al. 1990) so it is not surprising that pyroxene from all Apollo 17 basalts, including 71597, create a touching framework of crystals (Fig. 3). In comparison, the plagioclase analysis closest to the touching framework line (P = ~75%, R = 1.1) is from the equilibrated basalt 75015,52, which has the highest abundance of plagioclase (25 vol%) of the Apollo 17 basalts reported by Donohue and Neal (2015). Relative to other Apollo 17 basalts, plagioclase in 75015 has a lower calculated porosity (Fig. 3), consistent with compaction or overgrowth (e.g., Jerram et al. 1996, 2003). Olivine in 71597,12 has the lowest R (0.59) of any phase, and is the sole non-pyroxene phase to create a touching crystal framework (Fig. 3). Compared to other high-Ti basalt olivine, the 71597 olivine SDP is offset to a lower R and decreased porosity. This is an indication of increased poor sorting (i.e., accumulation), an interpretation further supported by the kinked olivine CSD reflecting two olivine crystal size populations (Fig. 2a). The combination of SDP and CSD analyses support the observation that olivine accumulation occurred as clusters in 71597 but was not a significant factor in any other high-Ti basalt (cf. Neal et al. 1990; Donohue and Neal 2015).

Crystal size distribution characteristics (CSD profile slope, y-intercept, and linearity) vary between phases (Fig. 2). However, direct comparisons first require accounting for variable growth rates of the different phases to estimate residence time of the different crystal cargoes present in 71597. It was noted above that growth rates are variable and are dependent on many factors that

change as a magma crystallizes, which leads to residence times with large errors. We can, however, estimate relative residence times simply by examining the gradients of the CSD profiles. For olivine and ilmenite, the CSDs are divided into two segments. Warner et al. (1977) suggested there was some ilmenite accumulation in 71597, and here the CSD has been subdivided at ~1 mm size bin. The populations of larger olivine and ilmenite crystals have the lowest CSD gradients (–2.8 ± 0.3 and –1.5 ± 0.1, respectively), indicating relatively longer residence times relative to other phases in 71597. This is consistent with the either prolonged olivine and ilmenite crystallization or accumulation of these phases.

The variation in modal olivine between our analysis and that of Warner et al. (1977) and Neal and Taylor (1993) indicates heterogeneous distribution of olivine at the thin section scale, consistent with crystal accumulation, possibly as clusters of olivine. The bimodal Fo-content distribution between large and matrix olivine (Fig. 5) is also consistent with accumulation in an evolving melt. Furthermore, compositional data suggest accumulation from a fractionating magma rather than from different magma batches, as there is no evidence of an antecryst origin for some olivines or for mixing between magmas with olivine on the liquidus. Olivine compositions also suggest that ilmenite was co-crystallizing with those containing the highest Fo contents, but ceased crystallizing around Fo_{69} (Fig. 6a).

The crystallization sequence and conditions for 71597 derived from textural analysis are consistent with sample geochemistry. The general sequence of crystallization is olivine + armalcolite → olivine + ilmenite → ilmenite + augite → ilmenite + augite + plagioclase → pigeonite + plagioclase. The CSDs and general textures indicate olivine crystallized first at an initial cooling rate of 1–3 °C per hour (cf. Usselman et al. 1975; Usselman and Lofgren 1976; Donohue and Neal 2015). Olivine and ilmenite were on the liquidus prior to eruption, and some matrix olivines likely crystallized at the surface. Ilmenite contains relatively high MgO contents (3.2–5.2 wt% MgO here, up to 8 wt% noted by Warner et al. 1977) compared to other Apollo 17 high-Ti basalts (0.17–4.87 wt% MgO), which may have resulted from reaction with the evolving melt during crystallization. This reaction is supported by abundant exsolution lamellae similar to those found in other re-equilibrated ilmenite from Apollo 17 basalts (e.g., El Goresy and Ramdohr 1975). This relatively high-Mg content in ilmenite is likely buffered by olivine resorption, with titanaugite and high-Ca plagioclase crystallization lowering CaO in the residual melt (as evidenced by decreasing CaO content in plagioclase with decreasing compatible element abundance) and leading to late pigeonite crystallization. There may also be a contribution from isothermal diffusion, which can inhibit Fe-enrichment commonly observed during pyroxene crystallization (e.g., Dungan and Brown 1977).

Type source of 71597

Mineral compositions and CSDs can be used to evaluate not only crystallization history but also source characteristics (e.g., Hui et al. 2011). Apollo 17 basalt 71597 is currently unclassified (being part of the "Type U" classification of Rhodes et al. 1976) because of the coarse grain size and small sample mass (12.35 g; Neal and Taylor 1993) making a representative whole-

rock analysis difficult to produce. This is why the whole-rock data reported by Murali et al. (1977) cannot be used to classify 71597. According to Haskin and Korotev (1977), Haskin et al. (1977), and Ryder and Schuraytz (2001), coarse-grained samples require up to 5 g of sample to be powdered to obtain a representative WR analysis. This would require consuming almost half of the original 12.35 g that comprised 71597. Murali et al. (1977) only used 0.612 g of this coarse-grained sample in their whole-rock analysis, strongly suggesting this is not representative of the true whole-rock composition. The data obtained as part of this study are used to propose a method for classifying 71597 within the chemical schemes already proposed, thus enhancing the science return on these precious samples.

Apollo 17 high-Ti basalts are separated into groups (Types A, B1, B2, C, D) based on whole-rock major and trace element abundances and ratios (Fig. 9; Rhodes et al. 1976; Neal et al. 1990; Ryder 1990). For example, the Type B basalt suite first identified by Rhodes et al. (1976), and later split into Types B1 and B2, were divided based on whole-rock rare earth element (REE) and high field strength element (HFSE) abundances and La/Sm ratios (Neal et al. 1990). Prior to the split, Warner et al. (1979) proposed 71597 originated in a thick high-Ti basalt flow

of Apollo 17 Type B basalt composition. The fraction of olivine in the bulk analysis has consequences for La, Sm, and Yb, which are controlled by the amount of mesostasis in the analysis (Haskin and Korotev 1977). However, ratios of these olivine-incompatible elements should be unaffected by olivine addition. Olivine (± ilmenite) accumulation should only dilute, and not fractionate, elements incompatible in olivine (and ilmenite—e.g., REEs). We attempted to distinguish the Apollo 17 high-Ti basalt source group for 71597 by accounting for trace element variation caused by olivine accumulation. The reported La/Yb ratio (0.63; Murali et al. 1977; Warner et al. 1977) is similar to Type B1 basalts, while the La/Sm ratio (0.77) is consistent with Type B2 basalts (Figs. 9b and 9c). The Yb/Sm ratio (1.23) is higher than all other A17 high-Ti basalts (0.83–1.13). Uncertainty in the INAA-determined REE abundances reported by Murali et al. (1977) are given only in general terms of ±1–5%. With this consideration, the Yb/Sm ratio of 71597 may then be within uncertainty of the upper limit of Type B1 basalts. However, calculated pre-cumulate values for 71597 yield compositions outside any Apollo 17 group (Fig. 9b), Type B2 basalts (Fig. 9c), and Type B1 basalts (Fig. 9d). The conflicting groupings and unique ratios of 71597 indicate at least some incompatible element ratios are not representative of the whole-rock.
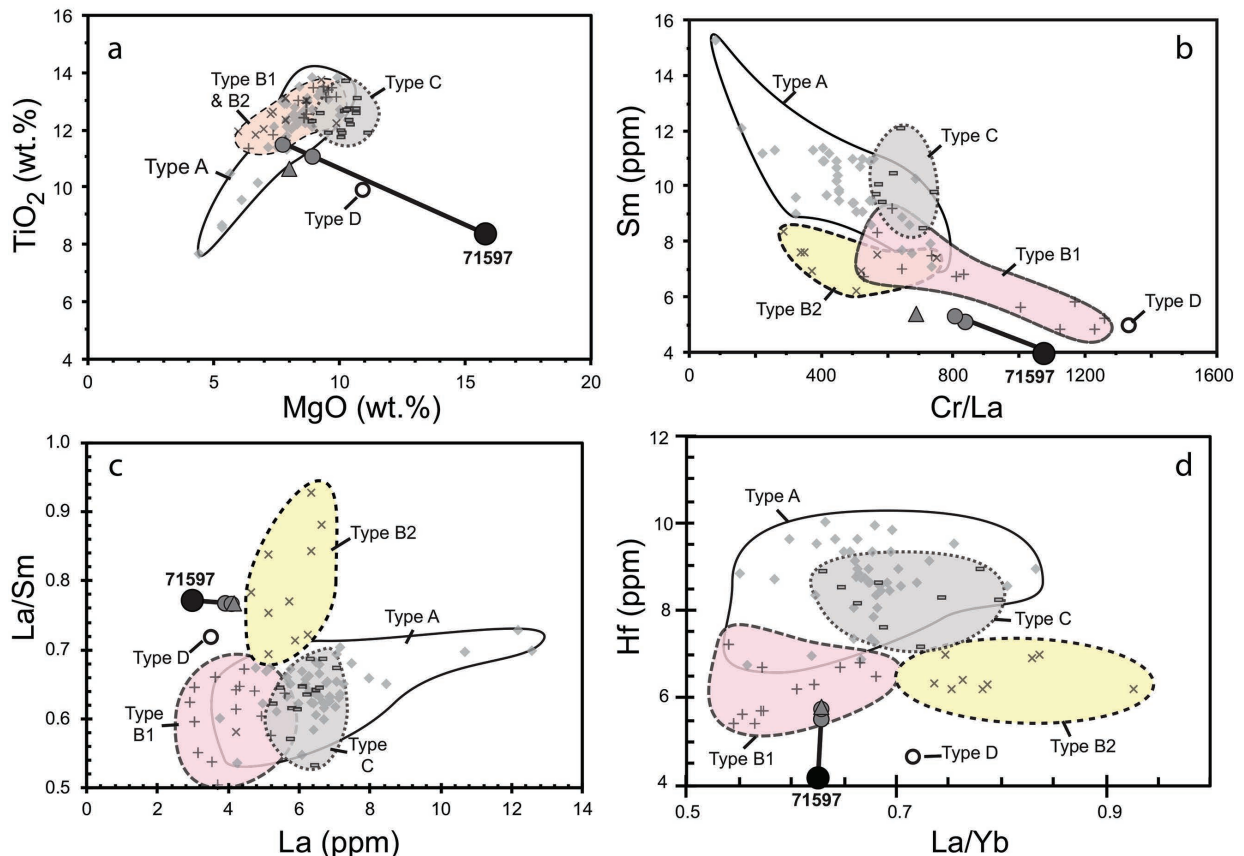

FIGURE 9. Compositional fields drawn from bulk-rock analyses of Apollo 17 high-Ti basalts of (**a**) TiO$_2$ (wt%) vs. MgO (wt%), (**b**) Sm (ppm) vs. Cr/La, (**c**) La/Sm vs. La (ppm), and (**d**) Hf (ppm) vs. La/Yb. Gray-shaded circles are compositions resulting from 24% (dark gray) and 27% (light gray) olivine subtraction from analysis of 71597,1 (black circle, Murali et al. 1977). Gray triangle represents subtraction of 27% olivine and 1% ilmenite. (Color online.)

TABLE 4. Results of fractionation calculations on 71597 composition

	71597,1[a]	Olivine	$D_{Ol/L}$	$D_{ilm/L}$	olivine (±ilmenite) subtraction		
wt%					24% ol	27% ol	27% ol + 1% ilm
SiO_2	39.2	37.9			39.61	39.68	40.44
TiO_2	8.4	0.047			11.03	11.48	10.60
Al_2O_3	7.9				10.39	10.82	10.97
Cr_2O_3	0.47	0.22			0.55	0.56	0.56
FeO	19.8	24.3			18.49	18.26	17.84
MnO	0.237	0.26			0.23	0.23	0.23
MgO	15.8	37.1			8.96	7.79	8.03
CaO	7.9	0.26			10.31	10.72	10.87
Na_2O	0.29				0.38	0.40	0.40
K_2O	0.027				0.04	0.04	0.04
Total	100	100.09			99.99	99.99	99.99
				ppm			
Cr	3216	1854	0.92	10	3292	3303	2849
Co	43	64	3.5	2.2	21	19	19
La	3	[0.01]	0.011	0.029	3.9	4.1	4.2
Sm	3.9	[0.01]	0.0002	0.053	5.1	5.3	5.4
Eu	1	[0.01]	0.007	0.02	1.3	1.4	1.4
Yb	4.8	[0.01]	0.030	0.051	6.3	6.5	6.6
Hf	4.2	[0.01]	0.010	0.38	5.5	5.7	5.8
Cr/La	1072				836	806	686
La/Sm	0.77				0.77	0.77	0.77
Yb/Sm	1.23				1.22	1.22	1.22

Notes: SiO_2 calculated to bring Total to 100. $D_{Ol/L}$ values from equations of Bédard (2005), assuming initial bulk MgO was 9 wt%. $D_{ilm/L}$ values from Haskin and Korotev (1977) except Hf (Klemme et al. 2006).
[a] INAA Values reported in Murali et al. (1977).

Major element oxide compositions of Apollo 17 high-Ti basalts group into trends (Fig. 9) that can be explained by simple fractional crystallization evolution (cf. Neal et al. 1990). Warner et al. (1977) showed that subtraction of 24–27% olivine from the measured 71597 bulk composition brought the sample into the range of other high-Ti basalts (cf. Table 4 of Warner et al. 1977). We expanded this model to include trace elements via Rayleigh fractionation. Incompatible trace element fractionation results (Table 4; Fig. 9) for removal of 24 or 27% olivine (±1% ilmenite) are essentially identical due to low olivine-melt and ilmenite-melt partition coefficients. The resultant trace element compositions once again yield conflicting classifications (Fig. 9). The La/Yb ratio is consistent with Type B1 basalts, while La/Sm is within the range of Type B2 basalts. The pre-cumulate abundances of La, Sm, and Cr are closest to Type B1 basalts. Modeled Yb and Eu abundances do not distinguish between Type B1 and B2 groups, and Co abundance is distinct only from Type B2 basalts. Therefore, either cumulate 71597 resulted from accumulation in a new magma type, one or more of the INAA-determined REEs are not representative of the parent melt, or the simple model of olivine accumulation is insufficient. An argument for any of these three possibilities would remain equivocal if only bulk

FIGURE 10. Element variation diagrams for calculated equilibrium melts from crystal interiors (filled symbols) and rims (open symbols). (**a**) Mg# vs. V (ppm). (**b**) Cr/Y vs. Cr (ppm) with inferred magma compositional path shown (dashed line). (**c**) Chondrite-normalized pyroxene and plagioclase equilibrium melt REE profiles compared to reported whole-rock and olivine subtracted compositions. (**d**) La vs. Eu correlation of whole-rock compositions from each group, and equilibrium liquid compositions of augite, pigeonite, and plagioclase. Fractional crystallization (FC) paths for Types B1 and B2 basalts are from Neal et al. (1990) to 70% crystallization. Two analyses of high-REE plagioclase are not shown, as they represent extreme fractionation during late-stage cooling. Calculations for removal of 24% olivine and 27% olivine + 1% ilmenite (not shown) are within uncertainty of the –27% olivine on **c** and **d**. Open symbols in **a**, **b**, and **d** represent rim analyses. See literature for bulk La and Eu values (Masuda et al. 1974; Laul et al. 1975; Shih et al. 1975; Warner et al. 1975, 1979; Rhodes et al. 1976; Murali et al. 1977; Neal et al. 1990; Neal 2001).

TABLE 5. Mineral-melt partition coefficients used in modeling of 71597

	Olivine	Armalcolite	Ilmenite	Plagioclase	Augite	Pigeonite
V	0.49[a]	6.7[c]	3.4[c]	0.010[h]	1.1[k]	0.33[a]
Cr	0.91[a]	6.4[c]	10[g]	0.018–0.021[i]	3.3[i]	10[g]
La	0.011[a]	0.006[d]	0.029[g]	0.013–0.022[j]	0.05–0.14[i]	0.004–0.023[i]
Ce	0.008[a]	0.007[d]	0.035[g]	0.015–0.022[j]	0.08–0.18[i]	0.006–0.035[i]
Pr	0.006[b]	0.007[d]	0.041[g]	0.037[g]	0.12–0.22[i]	0.01–0.052[i]
Nd	0.005[a]	0.008[d]	0.047[g]	0.012–0.018[j]	0.2–0.30[i]	0.021–0.098[i]
Sm	0.0002[a]	0.008[d]	0.053[g]	0.009–0.013[j]	0.24–0.33[i]	0.028–0.124[i]
Eu	0.007[a]	0.006[d]	0.020[g]	0.817–0.916[j]	0.26–0.36[i]	0.036–0.150[i]
Gd	0.004[a]	0.013[e]	0.081[g]	0.012[j]	0.28–0.37[i]	0.045–0.177[i]
Tb	0.01[a]	0.024[d]	0.095[g]	0.012[g]	0.29–0.38[i]	0.056–0.206[i]
Dy	0.01[a]	0.035[d]	0.013[c]	0.012[g]	0.29–0.40[i]	0.068–0.234[i]
Ho	0.016[a]	0.045[d]	0.018[c]	0.012[g]	0.29–0.43[i]	0.079–0.259[i]
Er	0.023[a]	0.056[d]	0.024[c]	0.001–0.004[j]	0.29–0.46[i]	0.09–0.280[i]
Tm	0.026[b]	0.060[f]	0.331[g]	0.012[g]	0.28–0.47[i]	0.1–0.297[i]
Yb	0.030[a]	0.070[d]	0.051[c]	0.012[g]	0.27–0.49[i]	0.109–0.310[i]
Lu	0.053[a]	0.070[e]	0.067[c]	0.011[g]	0.26–0.49[i]	0.117–0.321[i]

[a] Bédard (2005); [b] interpolated; [c] Dygert et al. (2013); [d] Neal et al. (1990); [e] Klemme et al. (2006); [f] Irving et al. (1978); [g] Haskin and Korotev (1977); [h] Bindeman et al. (1998); [i] RTlnD; [j] Hui et al. (2011); [k] Mallmann and O'Neill (2009); [l] Sun and Liang (2012).

whole-rock analyses were considered.

Equilibrium melt calculations theoretically yield compositions wherein mineral phases crystallized. Melt compositions (Fig. 10) were calculated for each phase by dividing trace element abundances by mineral-specific partition coefficients for V, Cr, and the REEs (Table 5). Olivine partition coefficients were calculated using the relationship of D to bulk MgO of Bédard (2005). Other partition coefficients were determined at low f_{O_2} (between IW-0 and IW-2) and with trace elements present at natural abundances (see references in Table 5). Equilibrium melts could be explained by a model in which fractional crystallization evolution is modified by olivine resorption (Fig. 10b). Equilibrium liquid compositions calculated from the cores of augite are similar to light REEs (LREE) or elevated above the heavy REEs (HREE) compared to whole-rock values from Murali et al. (1977) (Fig. 10c). The LREEs are more incompatible than HREEs in olivine, and so this discrepancy may result from an unaccounted for dilution of LREEs by olivine addition. Pigeonite equilibrium melts are similar to the compositional dispersion observed in plagioclase (Fig. 10c), but the majority are depleted in Eu, as seen on Figure 10d. Pigeonite likely originated in olivine reaction rims after plagioclase crystallized, which limited available Eu. Plagioclase equilibrium compositions follow the expected positive correlation between La and Eu (Fig. 10d).

Apollo 17 high-Ti basalts are classified primarily based on whole-rock trace element compositional variation. The trace elements obtained for olivine in 71597 are similar to olivines found in other chemical groups. In addition, the paucity of olivine in Type B1 basalts is not conducive to such comparisons. Here, we utilize augite to trace source evolution, because augite crystallizes early in high-Ti basalts, and has sufficient incompatible trace element abundance for quantification by LA-ICP-MS analyses. On Figure 10d, the whole-rock fractionation trends of La and Eu in Apollo 17 high-Ti basalts are compared to the plagioclase and pyroxene equilibrium liquids. Pigeonite, as might be expected from a phase appearing late in the crystallization sequence after modification by partial resorption, does not appear to represent true liquid composition. Finally, the evolution from augite equilibrium melt to relatively late-stage plagioclase most closely follows a fractional crystallization trend from a Type B2 basalt source composition.

IMPLICATIONS

Approximately one-third of high-Ti mare basalts returned by the Apollo 17 mission are designated as Type U or "unclassified" basalts. These have remained unclassified for 40+ years due to issues with obtaining representative bulk analyses, primarily due to small sample masses and coarse grain sizes. The approach used here has the potential to place petrogenetic constraints on these samples, and it has demonstrated potential for classification and discrimination of Type U basalts within the current whole-rock classification scheme for Apollo 17 high-Ti basalts, as well as potentially identifying new basalt types. The Earth and the Moon share many similarities in eruption styles of basalts. The characterization of end-member samples like 71597 will be important for comparative analyses with the growing collection of mare basalt textures that have been defined through quantitative analysis. Finally, application of these microscale techniques will maximize the science potential of future robotic sample return missions to the Moon and other planetary bodies.

Our work allows a unique Apollo sample to be tied to the Type B2 mare basalt suite. The Type B2 suite comprises nine fine-grained vitrophyric-olivine porphyritic basalts, and one plagioclase poikilitic basalt. We are not able to determine where olivine accumulation occurred, but it could have happened at the base of or in the lunar crust, or within a thick high-Ti basalt flow. If on the other hand, the cumulates formed within a given low, then we would expect more coarse-grained material represented in the Type B2 sample suite, which might be present but unrecognized in the Apollo sample collection.

REFERENCES CITED

Alexander, L., Snape, J.F., Crawford, I.A., Joy, K.H., and Downes, H. (2014) Searching for nonlocal lithologies in the Apollo 12 regolith: A geochemical and petrological study of basaltic coarse fines from the Apollo lunarsoil sample

12023,155. Meteoritics & Planetary Science, 49, 1288–1304.

Bédard, J.H. (2005) Partitioning coefficients between olivine and silicate melts. Lithos, 83, 394–419.

Bindeman, I.N., Davis, A.M., and Drake, M.J. (1998) Ion microprobe study of plagioclase-basalt partition experiments at natural concentration levels of trace elements. Geochimica et Cosmochimica Acta, 62, 1175–1193.

Burkhard, D.J.M. (2005) Nucleation and growth rates of pyroxene, plagioclase, and Fe-Ti oxides in basalt under atmospheric conditions. European Journal of Mineralogy, 17, 675–686.

Cabane, H., Laporte, D., and Provost, A. (2005) An experimental study of Ostwald ripening of olivine and plagioclase in silicate melts: Implications for the growth and size of crystals in magmas. Contributions to Mineralogy and Petrology, 150, 37–53.

Cashman, K.V., and Marsh, B.D. (1988) Crystal size distribution (CSD) in rocks and the kinetics and dynamics of crystallization II: Makaopuhi lava lake. Contributions to Mineralogy and Petrology, 99, 292–305.

Cushing, J.A., Taylor, G.J., Norman, M.D., and Keil, K. (1999) The granulitic impactite suite: Impact melts and metamorphic breccias of the early lunar crust. Meteoritics & Planetary Science, 34, 185–195.

Day, J.M.D., and Taylor, L.A. (2007) On the structure of mare basalt lava flows from textural analysis of the LaPaz Icefield and Northwest Africa 032 lunar meteorites. Meteoritics & Planetary Science, 42, 3–17.

Delano, J.W. (1980) Chemistry and liquidus phase relations of Apollo 15 red glass: Implications for the deep lunar interior. Proceedings of the 11th Lunar and Planetary Science Conference, 251–288.

Donohue, P.H., and Neal, C.R. (2015) Quantitative textural analysis of ilmenite in Apollo 17 high-titanium mare basalts. Geochimica et Cosmochimica Acta, 149, 115–130.

Dungan, M.A., and Brown, R.W. (1977) The petrology of the Apollo 12 ilmenite basalt suite. Proceedings of the 8th Lunar Science Conference, 1339–1381.

Dygert, N., Liang, Y., and Hess, P.C. (2013) The importance of melt TiO_2 in affecting major and trace element partitioning between Fe-Ti oxides and lunar picritic glass melts. Geochimica et Cosmochimica Acta, 106, 134–151.

Dymek, R.F., Albee, A.L., and Chodos, A.A. (1975) Comparative mineralogy and petrology of Apollo 17 mare basalts: Samples 70215, 71055, 74255, and 75055. Proceedings of the 6th Lunar Science Conference, 49–77.

El Goresy, A., and Ramdohr, P. (1975) Subsolidus reduction of lunar opaque oxides: Textures, assemblages, geochemistry, and evidence for a late-stage endogenic gaseous mixture. Proceedings of the 6th Lunar Science Conference, 729–745.

Fagan, A.L., Neal, C.R., Simonetti, A., Donohue, P.H., and O'Sullivan, K.M. (2013) Distinguishing between Apollo 14 impact melt and pristine mare basalt samples by geochemical and textural analyses of olivine. Geochimica et Cosmochimica Acta, 106, 429–445.

Hallis, L.J., Anand, M., and Strekopytov, S. (2014) Trace-element modelling of mare basalt parental melts: Implications for a heterogeneous lunar mantle. Geochimica et Cosmochimica Acta, 134, 289–316.

Haskin, L.A., and Korotev, R.L. (1977) Test of a model for trace element partition during closed-system solidification of a silicate liquid. Geochimica et Cosmochimica Acta, 41, 921–939.

Haskin, L.A., Jacobs, J.W., Brannon, J.C., and Haskin, M.A. (1977) Compositional dispersions in lunar and terrestrial basalts. Proceedings of the 8th Lunar and Planetary Science Conference, 1731–1750.

Higgins, M.D. (2000) Measurement of crystal size distributions. American Mineralogist, 85, 1105–1116.

——— (2002) Closure in crystal size distributions (CSD), verification of CSD calculations, and the significance of CSD fans. American Mineralogist, 87, 171–175.

——— (2006) Verification of ideal semi-logarithmic, lognormal or fractal crystal size distributions from 2D datasets. Journal of Volcanology and Geothermal Research, 154, 8–16.

Higgins, M.D., and Roberge, J. (2003) Crystal size distribution of plagioclase and amphibole from Soufrière Hills Volcano, Montserrat: Evidence for dynamic crystallization–textural coarsening cycles. Journal of Petrology, 44, 1401–1411.

Hodges, F.N., and Kushiro, I. (1974) Apollo 17 petrology and experimental determination of differentiation sequences in model moon compositions. Proceedings of the 5th Lunar Conference, 505–520.

Hui, H., Oshrin, J.G., and Neal, C.R. (2011) Investigation into the petrogenesis of Apollo 14 high-Al basaltic melts through crystal stratigraphy of plagioclase. Geochimica et Cosmochimica Acta, 75, 6439–6460.

Irving, A.J., Merrill, R.B. and Singleton, D.E. (1978) Experimental partitioning of rare earth elements and scandium among armalcolite, ilmenite, olivine and mare basalt liquid. Proceedings of the 9th Lunar and Planetary Science Conference, 601–612.

Jerram, D.A., Cheadle, M.J., Hunter, R.H., and Elliott, M.T. (1996) The spatial distribution of grains and crystals in rocks. Contributions to Mineralogy and Petrology, 125, 60–74.

Jerram, D.A., Cheadle, M.J., and Philpotts, A.R. (2003) Quantifying the building blocks of igneous rocks: Are clustered crystal frameworks the foundation? Journal of Petrology, 44, 2033–2051.

Jerram, D.A., Davis, G.R., Mock, A., Charrier, A., and Marsh, B.D. (2010) Quantifying 3D crystal populations, packing and layering in shallow intrusions: A case study from the Basement Sill, Dry Valleys, Antarctica. Geosphere, 6, 537–548.

Jolliff, B.L., Korotev, R.L., Zeigler, R.A., and Floss, C. (2003) Northwest Africa 773: Lunar mare breccia with a shallow-formed olivine-cumulate component, inferred very-low-Ti (VLT) heritage, and a KREEP connection. Geochimica et Cosmochimica Acta, 67, 4857–4879.

Klemme, S., Günther, D., Hametner, K., Prowatke, S., and Zack, T. (2006) The partitioning of trace elements between ilmenite, ulvospinel, armalcolite and silicate melts with implications for the early differentiation of the moon. Chemical Geology, 234, 251–263.

Laul, J.C., Schmitt, R.A., Robyn, M., and Goles, G.G. (1975) Chemical Composition of 18 Apollo 17 Rake Basalts and One Basalt Breccia. Proceedings of the 6th Lunar and Planetary Science Conference, 492–493.

Longhi, J., Walker, D., and Hays, J.F. (1978) The distribution of Fe and Mg between olivine and lunar basaltic liquids. Geochimica et Cosmochimica Acta, 42, 1545–1558.

Mallmann, G., and O'Neill, H.St.C. (2009) The crystal/melt partitioning of V during mantle melting as a function of oxygen fugacity compared with some other elements (Al, P, Ca, Sc, Ti, Cr, Fe, Ga, Y, Zr and Nb). Journal of Petrology, 50, 1765–1794.

Marsh, B.D. (1988) Crystal size distribution (CSD) in rocks and the kinetics and dynamics of crystallization I. Theory. Contributions to Mineralogy and Petrology, 99, 277–291.

——— (1998) On the interpretation of crystal size distributions in magmatic systems. Journal of Petrology, 39, 553–599.

Martin, V.M., Pyle, D.M., and Holness, M.B. (2006) The role of crystal frameworks in the preservation of enclaves during magma mixing. Earth and Planetary Science Letters, 248, 787–799.

Masuda, A., Tanaka, T., Nakamura, N., and Kurasawa, H. (1974) Possible REE anomalies of Apollo 17 REE patterns. Proceedings of the 5th Lunar Conference, 2, 1247–1253.

McCallum, I.S., and Charette, M.P. (1978) Zr and Nb partition coefficients: Implications for the genesis of mare basalts, KREEP, and sea floor basalts. Geochimica et Cosmochimica Acta, 42, 859–869.

McDonough, W.F., and Sun, S.-S. (1995) The composition of the Earth. Chemical Geology, 120, 223–253.

Morgan, D.J., and Jerram, D.A. (2006) On estimating crystal shape for crystal size distribution analysis. Journal of Volcanology and Geothermal Research, 154, 1–7.

Murali, A.V., Ma, M.-S., and Schmitt, R.A. (1977) Chemistry of 30 Apollo 17 rake basalts; 71597 a product of partial olivine accumulation. Abstracts of the 8th Lunar and Planetary Science Conference, 703–704.

Neal, C.R. (2001) Interior of the Moon: The presence of garnet in the primitive deep lunar mantle. Journal of Geophysical Research, 106, 27865–27886.

Neal, C.R., and Taylor, L.A. (1990) Modeling of lunar basalt petrogenesis: Sr isotope evidence from Apollo 14 high-alumina basalts. Proceedings of the 20th Lunar and Planetary Science Conference, 101–108.

——— (1993) Catalog of Apollo 17 Rocks Volume 2—Central Valley, Part 1, 472 pp. NASA.

Neal, C.R., Taylor, L.A., Hughes, S.S., and Schmitt, R.A. (1990) The significance of fractional crystallization in the petrogenesis of Apollo 17 Type A and B high-Ti basalts. Geochimica et Cosmochimica Acta, 54, 1817–1833.

Neal, C.R., Hacker, M.D., Snyder, G.A., Taylor, L.A., Liu, Y.-G., and Schmitt, R.A. (1994) Basalt generation at the Apollo 12 site, Part 2: Source heterogeneity, multiple melts, and crustal contamination. Meteoritics, 29, 349–361.

Neal, C.R., Donohue, P.H., Fagan, A.L., O'Sullivan, K.M., Oshrin, J., and Roberts, S. (2015) Distinguishing between basalts produced by endogenic volcanism and impact processes: A non-destructive method using quantitative petrography of lunar basaltic samples. Geochimica et Cosmochimica Acta, 148, 62–80.

Papike, J.J., Bence, A.E., and Lindsley, D.H. (1974) Mare basalts from the Taurus-Littrow region of the moon. Proceedings of the 5th Lunar Conference, 471–504.

Papike, J.J., Hodges, F.N., Bence, A.E., Cameron, M., and Rhodes, J.M. (1976) Mare basalts: Crystal chemistry, mineralogy, and petrology. Reviews of Geophysics and Space Physics, 14, 475–540.

Pearce, N.J., Perkins, W.T., Westgate, J.A., Gorton, M.P., Jackson, S.E., Neal, C.R., and Chenery, S.P. (1997) A compilation of new and published major and trace element data for NIST SRM 610 and NIST SRM 612 glass reference materials. Geostandards Newsletter, 21, 115–144.

Rhodes, J.M., Hubbard, N.J., Wiesmann, H., Rodgers, K.V., Brannon, J.C., and Bansal, B.M. (1976) Chemistry, classification, and petrogenesis of Apollo 17 mare basalts. Proceedings of the 7th Lunar Science Conference, 1467–1489.

Rhodes, J.M., Brannon, J.C., Rodgers, K.V., Blanchard, D.P., and Dungan, M.A. (1977) Chemistry of Apollo 12 mare basalts: Magma types and fractionation processes. Proceedings of the 8th Lunar Science Conference, 1305–1338.

Ryder, G. (1985) Catalog of Apollo 15 Rocks Part 2. 15306-15468. Curatorial Branch Publication, 72, 443 pp. NASA.

——— (1990) A distinct variant of high-titanium mare basalt from the Van Serg core, Apollo 17 landing site. Meteoritics, 25, 249–258.

Ryder, G., and Schuraytz, B.C. (2001) Chemical variation of the large Apollo 15 olivine-normative mare basalt rock samples. Journal of Geophysical Research, 106, 1435–1451.

Schnare, D.W., Day, J.M.D., Norman, M.D., Liu, Y., and Taylor, L.A. (2008) A laser-ablation ICP-MS study of Apollo 15 low-titanium olivine-normative and quartz-normative mare basalts. Geochimica et Cosmochimica Acta, 72, 2556–2572.

Schneider, C.A., Rasband, W.S., and Eliceiri, K.W. (2012) NIH Image to ImageJ: 25 years of image analysis. Nature Methods, 9, 671–675.

Shih, C.-Y., Wiesmann, H., Bansal, B.M., Brannon, J.C., and Haskin, L.A. (1975) On the origin of high-Ti mare basalts. Proceedings of the 6th Lunar Science Conference, 1255–1285.

Stanin, F.T., and Taylor, L.A. (1980) Armalcolite: An oxygen fugacity indicator. Proceedings of the 11th Lunar and Planetary Science Conference, 117–124.

Sun, C., and Liang, Y. (2012) Distribution of REE between clinopyroxene and basaltic melt along a mantle adiabat: effects of major element composition, water, and temperature. Contributions to Mineralogy and Petrology, 163, 807–823.

Taylor, L.A., Shervais, J.W., Hunter, R.H., Shih, C.-Y., Bansal, B.M., Wooden, J.L., Nyquist, L.E., and Laul, L.C. (1983) Pre-4.2 AE mare-basalt volcanism in the lunar highlands. Earth and Planetary Science Letters, 66, 33–47.

Usselman, T.M., and Lofgren, G.E. (1976) The phase relations, textures, and mineral chemistries of high-titanium mare basalts as a function of oxygen fugacity and cooling rate. Proceedings of the 7th Lunar Science Conference, 1345–1363.

Usselman, T.M., Lofgren, G.E., Donaldson, C.H., and Williams, R.J. (1975) Experimentally reproduced textures and mineral chemistries of high-titanium mare basalts. Proceedings of the 6th Lunar Science Conference, 997–1020.

van Achterbergh, E., Ryan, C.G., Jackson, S.E., and Griffin, W.L. (2001) Data reduction software for LA-ICP-MS: Appendix. In P.J. Sylvester, Ed., Laser Ablation-ICP-Mass Spectrometry in the Earth Sciences: Principles and applications, 29, p. 239–243. Mineralogical Association of Canada, Short Course Series.

Vinet, N., and Higgins, M.D. (2010) Magma solidification processes beneath Kilauea Volcano, Hawaii: A quantitative textural and geochemical study of the 1969-1974 Mauna Ulu lavas. Journal of Petrology, 51, 1297–1332.

Vobecký, M., Frána, J., Bauer, J., Řanda, Z., Benada, J., and Kuncíř, J. (1971) Radioanalytical determination of elemental compositions of lunar samples.

Proceedings of the 2nd Lunar Science Conference, 2, 1291–1300.

Walker, D., Longhi, J., and Hays, J.F. (1976) Heterogeneity in titaniferous lunar basalts. Earth and Planetary Science Letters, 30, 27–36.

Warner, R.D., Keil, K., Prinz, M., Laul, J.C., Murali, A.V., and Schmitt, R.A. (1975) Mineralogy, petrology, and chemistry of mare basalts from Apollo 17 rake samples. Proceedings of the 6th Lunar Science Conference, 193–220.

Warner, R.D., Berkley, J.L., Mansker, W.L., Warren, R.G., and Keil, K. (1976a) Electron microprobe analyses of spinel, Fe-Ti oxides and metal from Apollo 17 rake sample mare basalts. Special Publication 16, UNM Institute of Meteoritics, Albuquerque, 114 pp.

Warner, R.D., Warren, R.G., Mansker, W.L., Berkley, J.L., and Keil, K. (1976b) Electron microprobe analyses of olivine, pyroxene and plagioclase from Apollo 17 rake sample mare basalts, Special Publication 15, UNM Institute of Meteoritics, Albuquerque, 121 pp.

Warner, R.D., Keil, K., and Taylor, G.J. (1977) Coarse-grained basalt 71597: A product of partial olivine accumulation. Proceedings of the 8th Lunar Science Conference, p. 1429–1442.

Warner, R.D., Taylor, G.J., Conrad, G.H., Northrop, H.R., Barker, S., Keil, K., Ma, M.-S., and Schmitt, R.A. (1979) Apollo 17 high-Ti mare basalts: New bulk compositional data, magma types, and petrogenesis. Proceedings of the 10th Lunar and Planetary Science Conference, p. 225–247.

Endnote:

[1]Deposit item AM-18-26173, Supplemental Table. Deposit items are free to all readers and found on the MSA web site, via the specific issue's Table of Contents (go to http://www.minsocam.org/MSA/AmMin/TOC/2018/Feb2018_data/Feb2018_data.html).